Accepted Article Preview: Published ahead of online publication

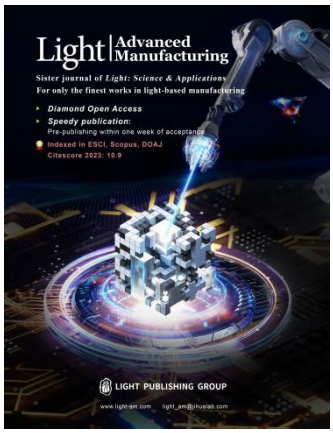

Dual-Band Hydrochromic Optical Modulator for Multimodal Anticounterfeiting and Encryption

Keunhyuk Ryu, Guanya Wang, ZhiLi Dong and Yi Long

Cite this article as: Keunhyuk Ryu, Guanya Wang, ZhiLi Dong, Yi Long. Dual-Band Hydrochromic Optical Modulator for Multimodal Anticounterfeiting and Encryption. *Light: Advanced Manufacturing* accepted article preview 7 May 2026; doi: 10.37188/lam.2026.079

Received 28 January 2026; revised 1 May 2026; accepted 6 May 2026;
Accepted article preview online 7 May 2026

Dual-Band Hydrochromic Optical Modulator for Multimodal Anticounterfeiting and Encryption

Keunhyuk Ryu[a,b], Guanya Wang[b], ZhiLi Dong[a,*], and Yi Long[b,*]

[a] School of Materials Science and Engineering, Nanyang Technological University, 639798, Singapore.

[b] Department of Electronic Engineering, The Chinese University of Hong Kong, New Territories, 999077, Hong Kong SAR, China.

*Corresponding authors.

E-mail addresses: ylong@ee.cuhk.edu.hk (Y. Long), ZLDong@ntu.edu.sg (Z. L. Dong)

<Abstract>

With the rise in digital threats and product counterfeiting, the development of advanced anticounterfeiting and encryption systems has become increasingly critical. Hydrochromic smart materials with dynamically tunable optical responses have emerged as a promising approach for next-generation anticounterfeiting applications. However, the vast majority of reported hydrochromic designs are based on single-band (visible) modulation, rendering them inherently vulnerable to decryption and replication. Herein, we address this challenge through the design of a controlled pore-structured hydrochromic dual-band anticounterfeiting platform, which enables multi-level information encoding across visible, mid-infrared, and attenuated total reflection Fourier-transform infrared modes, thereby enhancing authentication reliability. The platform is fabricated via a scalable and industrially compatible emulsion process and

exhibits dry–wet dual-band optical modulation superior to that of the state-of-the-art, achieving up to ~47.2% luminance transmittance modulation and ~0.55 mid-infrared emissivity modulation. Moreover, it demonstrates excellent environmental durability, maintaining stable optical performance after repeated dry–wet cycles and under harsh operating conditions, including high temperature, ultraviolet irradiation, and saltwater exposure, thereby ensuring long-term operational stability. The uniquely engineered hydrochromic dual-band anticounterfeiting platform offers a promising strategy for dynamically tuning optical responses across multiple wavelength regimes, with broad potential applications beyond advanced anticounterfeiting.

Keywords

Anticounterfeiting; Stimuli-Responsive Materials; Optical Modulator; Dual-Band Hydrochromic; Porous Structure

Introduction

Counterfeiting remains a critical global challenge that undermines the credibility of banknotes, pharmaceuticals, and consumer products, while also posing pronounced threats to economic stability, human health, and national security.[1-4] According to the Organisation for Economic Co-operation and Development–European Union Intellectual Property Office (OECD–EUIPO), counterfeit and pirated goods accounted for approximately USD 467 billion in global trade as of 2021.[5] Conventional single-level anticounterfeiting strategies, including quick response (QR) codes, stimulus-responsive inks, and digital authentication algorithms, suffer from limited dynamic reconfigurability and often rely on overly simplistic operating mechanisms.[6-9] Consequently, smart chromic materials capable of reversible and dynamic responses to external stimuli have emerged as promising candidates for next-generation information

encryption and anticounterfeiting applications.[10-13] Based on the type of external stimulus, these materials are broadly classified as thermo-, electro-, photo-, mechano-, and hydrochromic systems.[14-18] Among these, hydrochromic materials, characterised by optical modulation, such as a change in colour or transmittance induced by water immersion or humidity variation, offer unique advantages, including cost-effectiveness, environmental sustainability, and a sensible triggering mechanism, as water is one of the most abundant resources in nature.[19-23] Moreover, their stimulus-dependent optical responses under predefined water-related conditions enable condition-selective authentication without the need for external power sources or complex device integration. These attributes render hydrochromic smart materials particularly attractive for advanced information encryption and anticounterfeiting applications.

In general, the working principle of hydrochromic materials is exemplified by porous structures inspired by Diphylleia grayi, in which the degree of refractive index (n) matching governs optical switching between opaque and transparent states.[14, 24-26] Such water-triggered modulation is widely observed in natural systems and has further inspired the development of diverse bio-inspired hydrochromic designs. Previous hydrochromic smart materials have demonstrated rapid, real-time responsiveness,[20] excellent mechanical robustness,[21, 27] pronounced light-transmittance modulation (*e.g.*, luminance transmittance (T_{lum}, 360–780 nm) and solar transmittance (T_{sol}, 360–2500 nm)),[27] and fast switching speed.[28, 29] Nevertheless, most hydrochromic smart material systems remain restricted to single-band modulation (Figure 1a).[24-26, 30, 31] In particular, conventional hydrochromic designs often neglect the mid-infrared (MIR, 2.5–20 μm) region, thereby limiting their applicability in advanced anticounterfeiting scenarios and making them more vulnerable to decryption and replication. To address the growing demand for advanced anticounterfeiting technologies, real-world authenticity protection scenarios increasingly require multi-level protection schemes that enable authentication exclusively under specific stimuli or predefined conditions.

Herein, we report a rationally designed dual-band hydrochromic modulator (denoted as "dual-band modulator") that enables advanced multi-level anticounterfeiting (Figure 1b). The dual-band modulator-based anticounterfeiting platform operates in three distinct modes: In Level 1 (visible mode), the dual-band modulator switches from an opaque state to a transparent state upon exposure to water. In Level 2 (MIR mode), the device exhibits low MIR emissivity in the dry state and substantially higher MIR emissivity in the wet state, which can be clearly distinguished via IR imaging. In Level 3 (attenuated total reflection–Fourier transform infrared, ATR–FTIR mode), authentication is achieved through specific functional-group absorption features, which can only be reliably verified using expert-assisted ATR–FTIR spectroscopy. Through the integration of these hierarchical multi-level pathways, the device enables condition-specific authentication, thereby substantially improving resistance against counterfeiting attempts. The proposed device comprises a porous polymer, patterned polyethylene terephthalate (PET), an integrated low-emissivity (low-E) layer, and an underlying substrate, which can be manufactured via a facile water-in-oil (W/O) emulsion process followed by spin-coating (Figure 1c). Notably, the dual-band modulator exhibits pronounced optical contrast, achieving up to ~47.2% luminance transmittance modulation (ΔT_{lum}) and ~0.55 MIR emissivity modulation ($\Delta \varepsilon_{MIR}$) between the dry and wet states. It further demonstrates high operational durability, sustaining performance over 100 repeated dry–wet cycles and under stringent environmental conditions, including 80 °C and 60% RH, ultraviolet (UV) irradiation at 365 nm, and saltwater exposure for 20 days, while maintaining relatively consistent modulation behaviour. Building upon these characteristics and its simple fabrication process, the dual-band modulator-based anticounterfeiting device, featuring selective dual-band modulation and chemically addressable functional groups, represents a robust platform for advanced anticounterfeiting applications, while offering considerable potential for extension into next-generation smart optical and photonic systems.

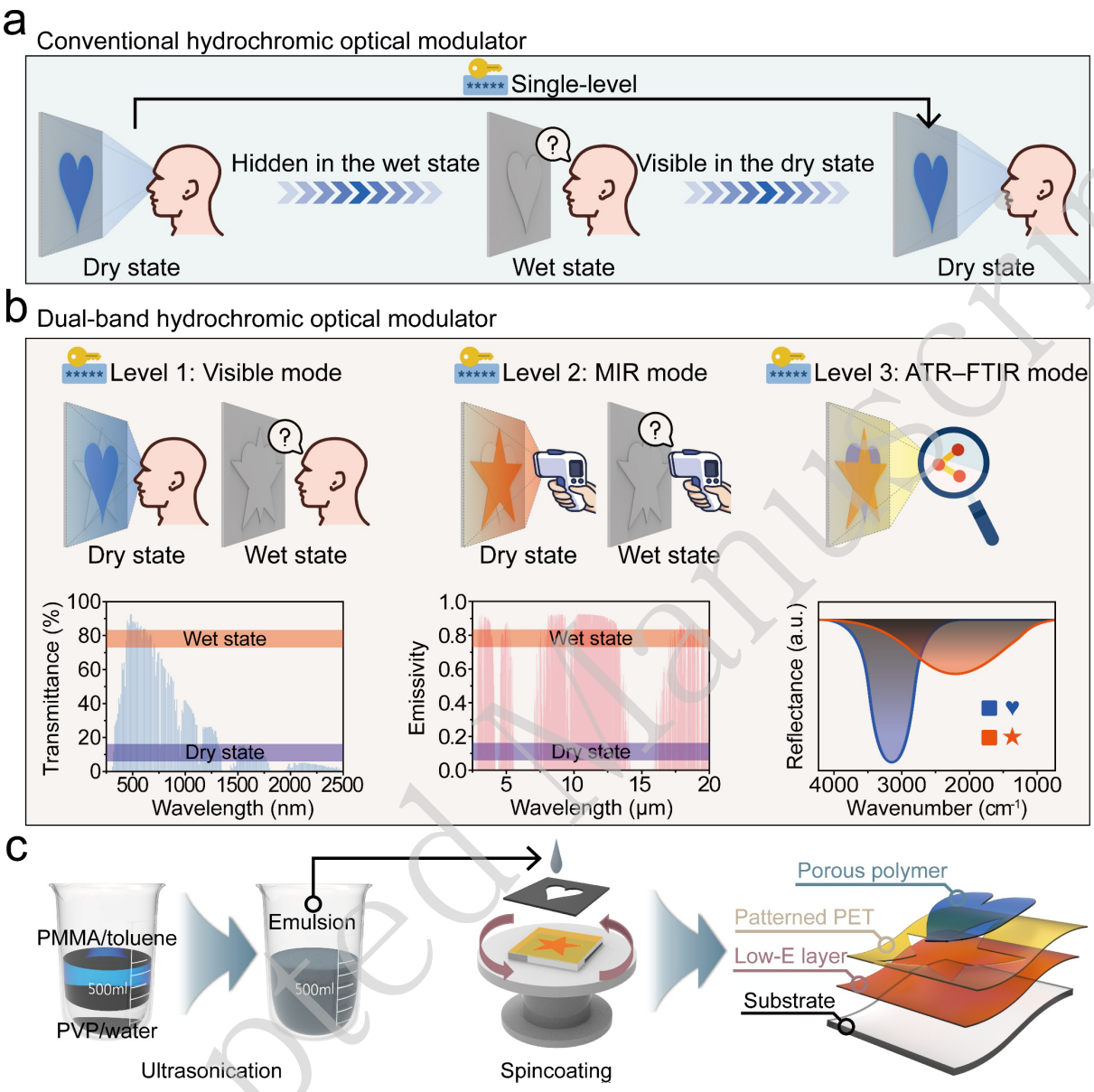

Figure 1. *(a) Schematic illustration of a conventional single-band hydrochromic optical modulator, which provides only a single level of anticounterfeiting functionality in the visible range. (b) Conceptual illustration of a dual-band hydrochromic optical modulator, enabling multi-level anticounterfeiting across the visible, MIR, and ATR–FTIR modes, with each mode selectively revealing different layers of information (the shaded blue and red regions represent the normalised AM1.5 global solar spectrum and the atmospheric transmittance window, respectively). (c) Schematic representation of the fabrication process for the dual-band modulator and the structural configuration of the final device.*

Results and Discussion

Porous Microstructure Evaluation and Dual-Band Optical Modulation Simulation

Poly(methyl methacrylate) (PMMA) dissolved in toluene and polyvinylpyrrolidone (PVP) dissolved in water are ultrasonicated for 4 h (Figure 1c) to form a stable emulsion, which is subsequently coated onto a low-E substrate, resulting in a structure composed of a porous polymer layer, a low-E layer, and the underlying substrate (Figure 2a(i)). Scanning electron microscopy (SEM) images reveal the microstructure of the porous polymer film as a function of PMMA concentration (Figures S1 and 2a(ii-vi)) after water evaporation. At ≤1 wt%, no discernible pores are observed (Figures S1 and 2a(ii)), which may be attributed to insufficient solid content to form a continuous porous polymer network. Initial pore formation is observed at 2 wt% (Figure 2a(iii)). From 4 wt%, the microstructure exhibits a marked increase in the number and size of pores, and the overall morphology remains similar between 4 wt% and 6 wt% (Figures 2a(iv) and 2a(v)). At 8 wt%, the characteristic pore size is similar to that at 4 wt% and 6 wt%, whereas the overall areal pore coverage decreases, presumably due to the excessive PMMA content leading to a denser matrix that limits pore formation (Figure 2a(vi)). Figure 2b summarises the evolution of pore area fraction and average pore size with PMMA concentration. Pore formation is first observed at 2 wt%, with a pore area fraction of ~40% and an average pore size of ~0.7 μm. The pore area fraction reaches a maximum at 4 wt% (~60%) and subsequently declines, reaching ~30% at 8 wt%. Meanwhile, the average pore size increases markedly at 4 wt% (~3.9 μm) and remains relatively constant over the range of 4 wt% to 8 wt% (~3.7 μm–3.9 μm). Relatively large error bars in the measured average pore size are observed at ≥4 wt%, likely due to the heterogeneous distribution of pore sizes. Moreover, increasing the number of coating layers results in a gradual decrease in surface porosity as surface pores become progressively covered (Figure S2). These quantitative trends are in good agreement with the SEM observations. Finite-difference time-domain (FDTD) simulations

further indicate that the device exhibits relatively low transmittance in the visible and near-infrared (NIR) regions (52.5% at 500 nm; 59.4% at 1000 nm) and maintains low emissivity ($\varepsilon_{MIR} \approx 0.40$ at 10 μm) in the dry state (Figure 2c). Conversely, upon wetting, the transmittance increases to 77.6% and 88.1% at 500 and 1000 nm, respectively, with ε_{MIR} increasing to 0.95. The electromagnetic field distributions at different wavelengths are presented in Figures 2d and 2e. Under the dry state, strong scattering of incident visible light (500 nm) and NIR (1000 nm) is observed within the structure, as evidenced by the high field intensities, which appear as near-red regions in Figures 2d(i) and 2d(ii). Conversely, when water infiltrates the pores, the reduced n contrast between PMMA (n = 1.49) and water (n = 1.33), compared with that between PMMA and air (n = 1.00), suppresses light scattering and promotes optical transmission. As a result, the field intensity decreases, as evidenced by the predominance of blue regions (Figures 2d(iii) and 2d(iv)). In the MIR regime, 10 μm radiation under the dry state is predominantly reflected in the FDTD simulation, as indicated by the high field intensity (near-red) observed within the structure (Figure 2e(i)), due to the MIR transparency of PMMA and the high reflectivity of the underlying low-E layer. By contrast, under the wet state, strong absorption of 10 μm radiation by water results in reduced field intensity (blue), as illustrated in Figure 2e(ii). These simulation results demonstrate the capability of the modulator to achieve simultaneous dual-band optical modulation.

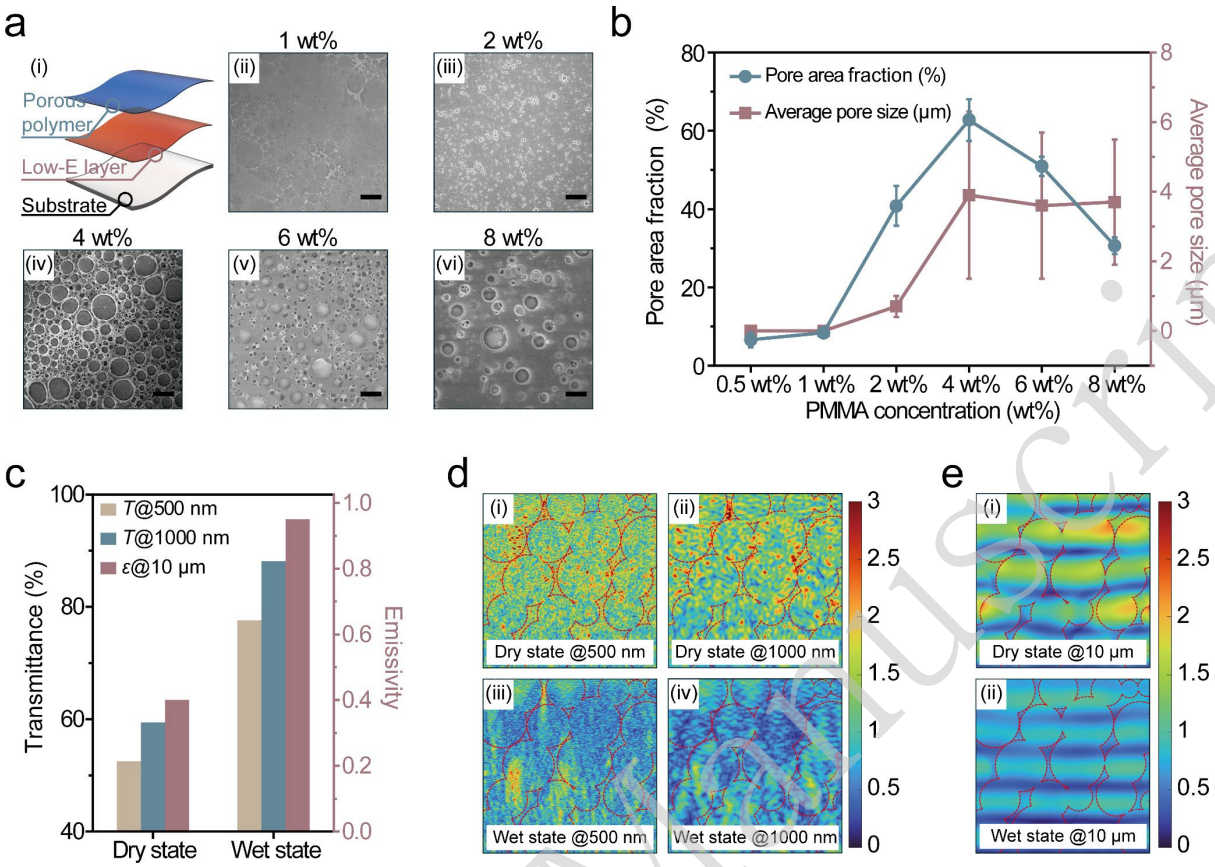

Figure 2. *(a) (i) Schematic illustration of the structure of the dual-band modulator and SEM images as a function of PMMA concentration: (ii) 1 wt%, (iii) 2 wt%, (iv) 4 wt%, (v) 6 wt%, and (vi) 8 wt% (scale bar: 10 μm). (b) Pore area fraction (%) and average pore size of porous PMMA films as a function of PMMA concentration. (c) FDTD simulation results illustrating transmittance and emissivity modulation behaviour of the dual-band modulator under dry and wet states. (d) Simulated electric field distributions illustrating light propagation at different wavelengths under dry and wet states (i) dry, 500 nm; (ii) dry, 1000 nm; (iii) wet, 500 nm; and (iv) wet, 1000 nm. (e) Simulated electric field distributions at a wavelength of 10 μm under (i) dry and (ii) wet states. The field maps display the lateral (x-axis) and depth (z-axis) directions, with colour representing relative electric field intensity, where red corresponds to higher intensity and blue to lower intensity. The red dotted line represents the porous structure.*

Optical–Thermal Modulation Performance of Dual-Band Modulator

Figure 3a demonstrates the optical performance of the dual-band modulator as a function of PMMA concentration. Samples with concentrations of 2 wt% or lower show the highest T_{lum} and T_{sol} values (74.1% and 71.7%) under the dry state. In the wet state, the T_{lum} and T_{sol} values of these samples increase only slightly (96.1% and 87.3%), indicating limited transmittance modulation due to insufficient pore formation. At 4 wt%, the T_{lum} and T_{sol} values decrease to 9.2% and 9.8% in the dry state, while increasing to 56.4% and 60.4% in the wet state, respectively. The modulation capability decreases for the 6 and 8 wt% samples, which may be attributed to reduced pore area, consistent with the microstructural observations (Figures S1, 2a, and 2b). This trend indicates that PMMA concentration governs the pore microstructure and, consequently, the optical performance of the device. At low PMMA concentration, insufficient polymer content limits pore formation, resulting in reduced dry–wet optical contrast. At high PMMA concentration, although pore size remains comparable, the decreased pore area fraction and increased polymer coverage suppress refractive-index contrast, leading to diminished transmittance modulation performance. Figure 3b presents the ultraviolet–visible–near infrared (UV–Vis–NIR) spectra of the dual-band modulator with 4 wt% PMMA under dry and wet states. The dual-band modulator shows the robust modulation of $\Delta T_{lum/sol}$ 47.2% and 50.6%, respectively. The photographs in Figure 3c confirm the visible modulation capability of the sample, revealing a clear optical contrast between the dry and wet states. The ε_{MIR} performance of the samples was systematically assessed as a function of PMMA concentration (Figure 3d). In the dry state, a consistently low ε_{MIR} value (~0.2) is maintained up to 2 wt%, and above 4 wt%, ε_{MIR} gradually increases, reaching a maximum of ~0.5 at 8 wt%. The increased dry state ε_{MIR} at higher PMMA concentrations is likely associated with increased polymer loading in the coating layer, which may reduce the reflectance contribution from the underlying low-E substrate. Meanwhile, across all samples in the wet state, consistently high emissivity of approximately 0.8 was observed, owing to the intrinsically high ε_{MIR} of water.[32]

Figure 3e demonstrates the ε_{MIR} modulation capability of the device, with the 4 wt% PMMA samples exhibiting a $\Delta\varepsilon_{MIR}$ of 0.55 between dry and wet states. The IR images visually confirm this $\Delta\varepsilon_{MIR}$ capability: in the dry state, the sample appears dark, indicating low ε_{MIR}, whereas in the wet state, the sample becomes brighter, indicating a marked increase in ε_{MIR} (Figure 3f). In addition to the pronounced dual-band contrast, the device exhibits fast, reversible switching behaviour between dry and wet states, as presented in Figure S3 and Video S1. Based on the balance between hydrochromic performance and $\Delta\varepsilon_{MIR}$, the optimal fabrication parameters, including a 4 wt% PMMA concentration, a single coating layer, and a spin-coating speed of 500 rpm, were selected for the dual-band modulator (Figures S4, S5, and S6). A comparison with hydrochromic optical modulators reported in previous studies is presented in Table S1, indicating that the present device achieves competitive optical performance while uniquely offering dual-band modulation functionality. The device exhibits highly consistent dual-band wavelength-responsive behaviour not only to direct water contact but also under varying relative humidity (RH). Figure 3g presents photographs and IR images of the device at different RH, showing that the transparency and ε_{MIR} increase progressively with increasing RH, as evidenced by the gradual enhancement of transparency in the photographs and the corresponding brightening observed in the IR images. Figures 3h(i) and 3h(ii) present contour maps of transmittance and emissivity across a range of wavelengths as a function of RH. Both visible transmittance and MIR emissivity progressively increase with rising RH, as indicated by a shift toward red regions in the contour plots. When the RH level is lowered from 80% to 50%, both transmittance and emissivity gradually decrease, as indicated by the shift toward blue regions, demonstrating a reversible dual-band response. The modulation exhibits a strong linear dependence on RH ($R^2 \approx 0.98$), indicating excellent humidity sensitivity (Figure S7) and highlighting its potential for application in optical humidity sensors and moisture-sensitive healthcare-related platforms. With its multiband modulation capability and excellent

reversibility, the dual-band modulator demonstrates a robust response to both direct water contact and ambient humidity, highlighting its broad applicability beyond anticounterfeiting, including next-generation smart optical and photonic systems.

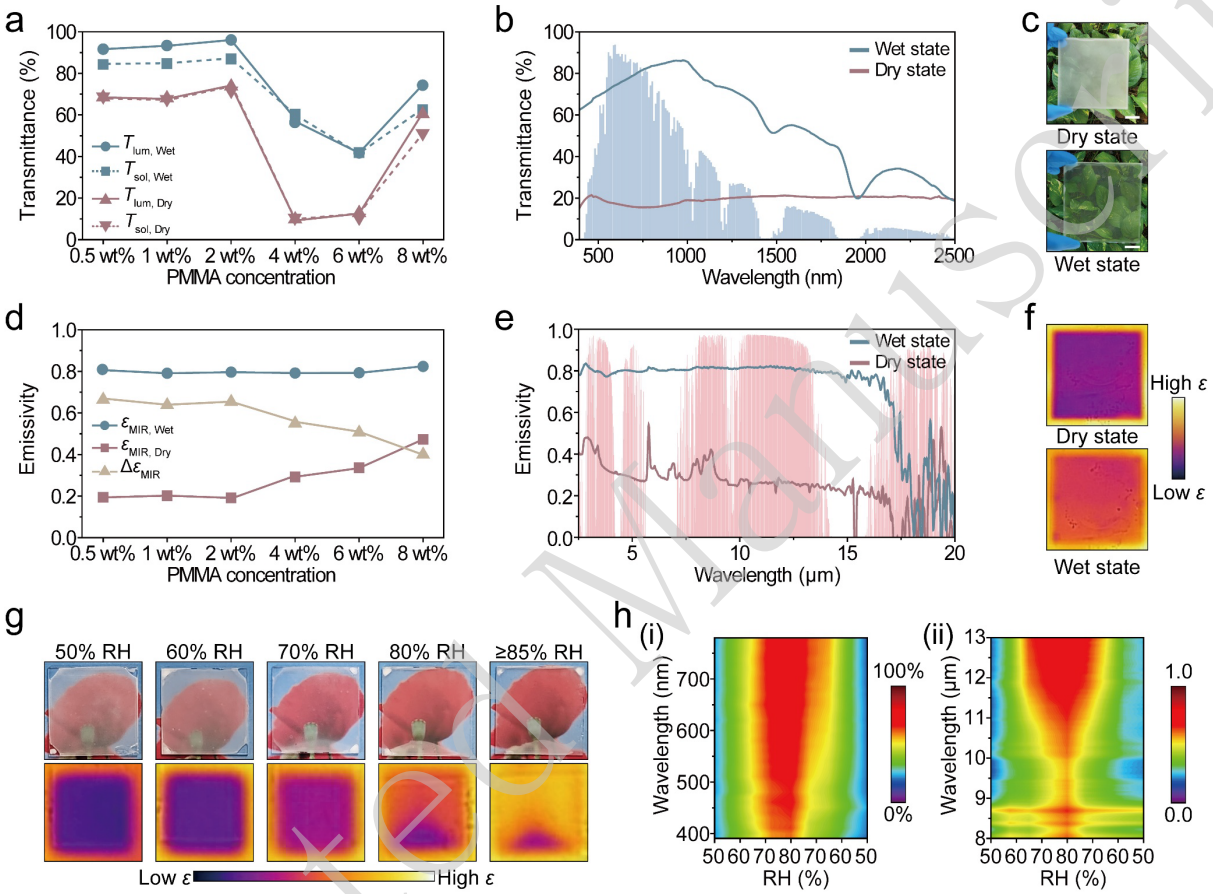

Figure 3. *(a) Optical transmittance of samples with varying PMMA concentrations in dry and wet states. (b) UV–Vis–NIR transmittance spectra of the 4 wt% PMMA sample in dry and wet states, overlaid with the normalised AM1.5 global solar spectrum (blue-shaded region). (c) Photographs of the 4 wt% PMMA sample in dry and wet states (scale bar: 2 cm). (d) Emissivity values of samples with different PMMA concentrations in dry and wet states. (e) Emissivity spectra of the 4 wt% PMMA sample in dry and wet states, shown together with the normalised AM1.5 atmospheric transmittance spectrum (red-shaded region). (f) IR images of the sample in dry and wet states. (g) Photographs and IR images of the 4 wt% PMMA sample under different RH conditions. (h) RH- and wavelength-resolved (i) transmittance contour map and (ii) emissivity contour map. The x-axis represents RH (%), the y-axis denotes*

wavelength, and the colour scale indicates (i) transmittance (%) and (ii) emissivity magnitude, with red indicating higher and blue indicating lower values.

Proof-of-Concept Demonstration of Multi-Level Anticounterfeiting

Leveraging the dual-band modulation capability of the proposed hydrochromic functional device, the dual-band modulator-based anticounterfeiting prototypes are fabricated, as shown in Figure 4. The facile spin-coating process described in Figure 1c enables versatile substrate selection, including flexible PET, which exhibits excellent mechanical resilience under folding (Figure 4a), thereby highlighting its suitability for flexible device applications. To demonstrate the multi-level anticounterfeiting capability, a conventional hydrochromic sample (serving as the control group) and the proposed prototype (*i.e.*, the dual-band modulator) with a distinct "★" pattern are prepared for direct comparison (Figure 4b). Both the control group and the dual-band modulator display opaque appearances with well-defined patterns under dry conditions (Figures 4b(i) and 4b(ii)). Conversely, under wet conditions, the pattern "★" becomes indistinct due to water-induced suppression of light scattering, yet reappears upon drying, thereby confirming reversible switching behaviour associated with Level 1 anticounterfeiting. Interestingly, the control group shows no discernible pattern in IR imaging due to the absence of a low-E layer (Figure 4c(i)), whereas the dual-band modulator displays a clearly resolved "★" pattern, with strong contrast between the low-E layer and the patterned PET, thereby demonstrating Level 2 anticounterfeiting functionality (Figure 4c(ii)). This comparison underscores the critical role of dual-band modulation in enabling multi-level anticounterfeiting, in contrast to conventional hydrochromic films that operate only in a single band. The device exhibits stable luminance transmittance modulation over 100 repeated dry–wet cycles (Figure 4d). Moreover, transmittance modulation remains stable for ~20 days under accelerated testing conditions, involving severe environmental stress, including continuous

heating at 80 °C and 60% RH, UV irradiation at 365 nm with an intensity equivalent to 1 sun, and exposure to 5 wt% saltwater (Figure 4e), while maintaining an uncompromised ΔT_{lum} value of ~40%, demonstrating durability comparable to that of high-performance energy-saving coatings.[33] This durability is partly attributed to the use of PMMA as the porous matrix, owing to its excellent UV resistance, thermal stability up to approximately 100 °C, and chemical stability in aqueous environments relative to other polymeric systems.[34] These results demonstrate the device's strong environmental durability and its practical potential for real-world deployment. Owing to the facile W/O emulsion combined with the spin-coating process, various patterns can be readily integrated within a single device (Figure 4f). As demonstrated, both the control group and the prototype exhibit a clear "♥" pattern in the dry state, which becomes visually distinguishable upon wetting, thereby corresponding to Level 1 anticounterfeiting based on visible optical contrast (Figures 4f(i) and 4f(ii)). Under IR imaging, however, the control group shows no discernible feature in either the dry or wet states, owing to the absence of a low-E layer, leading to uniformly high emissivity across the surface (Figure 4f(i)). In contrast, the dual-band modulator reveals a clearly defined dark "★" feature in the MIR mode under the dry state, while this feature becomes progressively less distinguishable upon wetting due to the high emissivity of water, thereby enabling Level 2 anticounterfeiting (Figure 4f(ii)). Figure 4g presents a comparative analysis of the optical spectra of the control group and the prototype. The control group demonstrates a large luminance transmittance modulation ($\Delta T_{lum} \approx 40\%$); however, its solar transmittance modulation remains limited ($\Delta T_{sol} \approx 35\%$), because the NIR transmittance is already high even in the dry state, primarily owing to the absence of the low-E layer (Figures 4g(i) and S8). Additionally, the absence of the low-E layer results in persistently elevated emissivity, leading to poor emissivity modulation capability, with $\Delta\varepsilon_{MIR}$ below ~0.1. As a result, the control group supports only Level 1 anticounterfeiting and does not provide the dual-band modulation necessary for Level 2 and

advanced anticounterfeiting functionalities. By contrast, the prototype exhibits robust dual-band modulation performance, achieving high ΔT_{lum} and ΔT_{sol} values of ~50%, together with a pronounced emissivity modulation of $\Delta\varepsilon_{MIR} \approx 0.52$ (Figures 4g(ii) and S8). This synergistic dual-band modulation spanning the visible and MIR spectral regions enables robust Level 2 anticounterfeiting under multiple optical wavelength channels. Furthermore, the prototype enables Level 3 anticounterfeiting through the identification of distinct characteristic functional groups, offering a chemically encoded security feature. ATR–FTIR analysis reveals characteristic vibrational absorption peaks of PMMA and PVP at ~2990 cm^{-1} (C–H stretching), ~1730 cm^{-1} (C=O stretching), ~1650 cm^{-1} (C=O stretching), and ~1147 cm^{-1} (–OCH_3 stretching). The control group exhibits significantly stronger PMMA- and PVP-related absorption features owing to the absence of the low-E layer, whereas these peaks are noticeably attenuated in the dual-band modulator (Figure 4h).[35-38] These distinct spectroscopic signatures enable unambiguous chemical differentiation between the two films. Collectively, these results demonstrate a proof-of-concept multi-level anticounterfeiting platform integrating Level 1 (visible mode), Level 2 (MIR mode), and Level 3 (ATR–FTIR mode) within a single dual-band hydrochromic architecture.

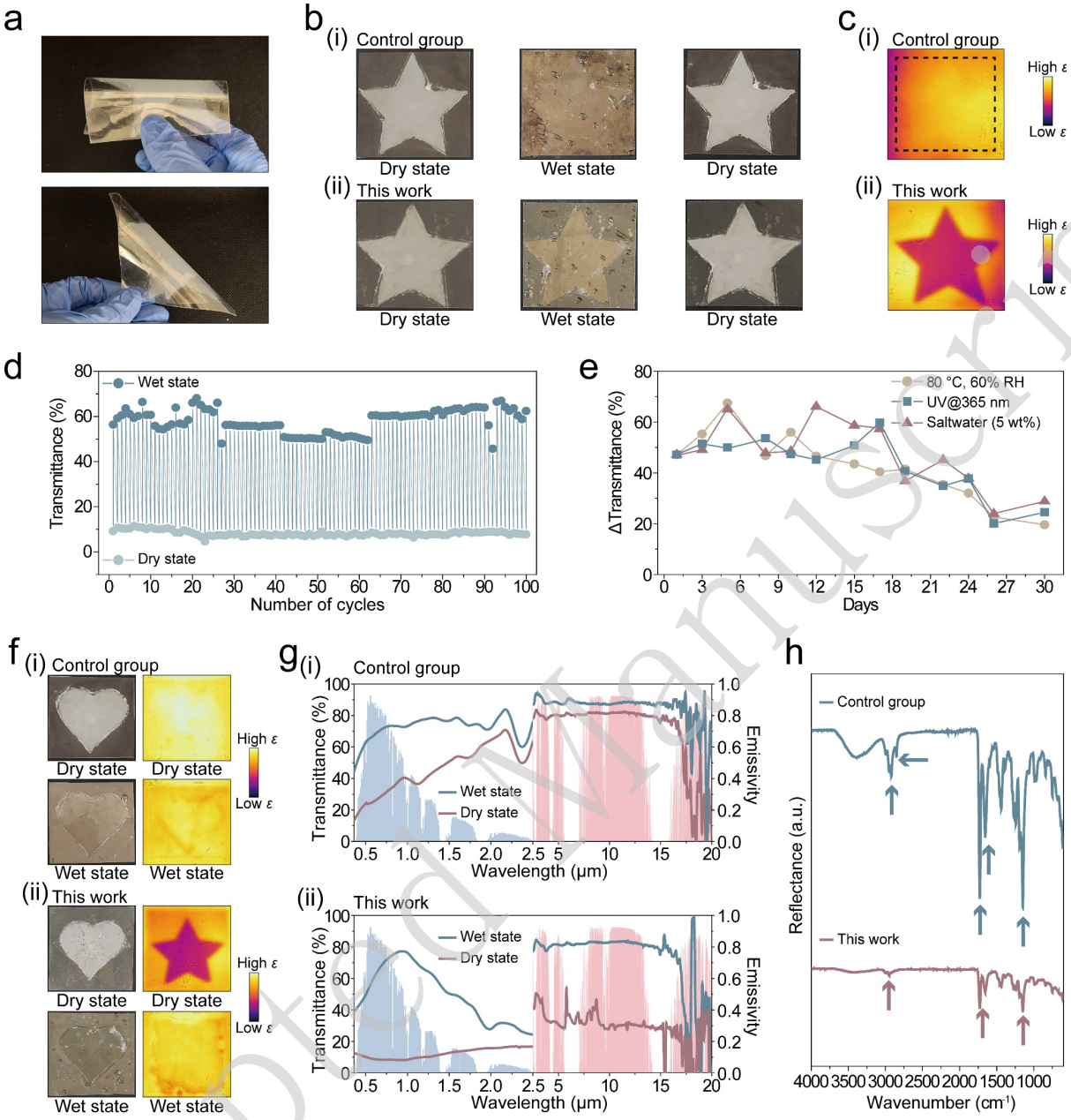

Figure 4. *(a) Photograph demonstrating the mechanical flexibility of the device. (b) Photographs of (i) the control group and (ii) the prototype in dry and wet states, and (c) corresponding IR images of (i) the control group and (ii) the prototype in dry state featuring a "★" pattern. (d) Cycling performance of the prototype under repeated drying and wetting cycles. (e) Evolution of* ΔT_{lum} *of the prototype during 30 days of accelerated ageing under three stressors, including high temperature (80 °C, 60% RH, yellow curve), 365 nm UV irradiation (blue curve), and 5 wt% saltwater exposure (red). (f) Photographs and IR images of (i) the control group with "♥" patterns and (ii) the prototype incorporating both "♥"*

and "★" patterns within a single device. (g) UV–Vis–NIR transmittance and emissivity spectra of (i) the control group and (ii) the prototype in dry and wet states, presented alongside the normalised AM1.5 global solar spectrum (blue shading) and the atmospheric transmittance window (red-shaded region). (h) ATR–FTIR reflectance spectra of the control and the prototype, with arrows representing characteristic vibrational absorption peaks.

Conclusion

In this study, we report a hydrochromic-based dual-band anticounterfeiting device that is capable of enabling multi-level authentication using visible, MIR, and ATR–FTIR modes. The device exhibits strong optical modulation (ΔT_{lum} of 47.2% and $\Delta\varepsilon_{MIR}$ of 0.55), as well as high sensitivity to both direct water contact and humidity variations. It also demonstrates excellent durability, sustaining stable modulation performance after 100 repeated dry–wet cycles and prolonged exposure to high temperature (80 °C and 60% RH), UV irradiation (365 nm), and saltwater (5 wt%). Benefiting from a facile and scalable W/O emulsion system combined with a spin-coating process, the device also allows for large-scale fabrication and flexible substrate compatibility, thereby enhancing its potential for practical deployment. Importantly, the device enables multi-level authentication: in Level 1 (visible mode), the dual-band modulator switches from an opaque state to a transparent state upon exposure to water; in Level 2 (MIR mode), the device exhibits low emissivity in the dry state and high emissivity in the wet state, which can be distinguished using IR imaging; and in Level 3 (ATR–FTIR mode), characteristic functional-group absorption signatures can be spectroscopically identified through expert-assisted ATR–FTIR analysis. Such a hierarchical design establishes a robust anticounterfeiting strategy in which authenticity can be validated only under predefined and orthogonal stimulus conditions, thereby significantly enhancing authentication security and reliability. The proposed design principle of hydrochromic dual-band modulation offers strong potential to

serve as a versatile platform for multi-level anticounterfeiting and provides a new pathway toward advanced anticounterfeiting and next-generation smart chromic technologies.

Materials and Methods

Materials

Glass substrates (2.5 cm × 2.5 cm, single-sided indium tin oxide (ITO)-coated, Winteck Technology) were utilised for performance optimisation, while polyethylene terephthalate (PET) substrates (10 cm × 10 cm, single-sided ITO-coated and pristine, Sigma-Aldrich) were used for anticounterfeiting prototypes. Bare PET film was employed as a masking layer for pattern information in the anticounterfeiting prototypes. Poly(methyl methacrylate) (PMMA, Mw ~120,000, Sigma-Aldrich), polyvinylpyrrolidone (PVP, Mw ~40,000, Sigma-Aldrich), deionised (D.I) water, ethanol (95%, Aik Moh), and toluene (anhydrous, 99.8%, Sigma-Aldrich) were used as received without any further purification.

Water-in-Oil (W/O) emulsion preparation

PMMA was selected as the porous matrix owing to its excellent compatibility with the W/O emulsion process, MIR transparency, and chemical stability. Accordingly, a series of PMMA solutions was prepared by dissolving 0.2 g, 0.45 g, 0.74 g, 1.55 g, 2.4 g, and 3.2 g of PMMA in 30 mL of toluene. Separately, a PVP aqueous solution was prepared by dissolving 0.5 g of PVP in 10 mL of D.I water. The two solutions were combined in a 60 mL vial and ultrasonicated for 4 h to form a stable and homogeneous W/O emulsion.

Dual-band optical modulator preparation

Glass substrates with a single-sided ITO coating were cleaned with ethanol prior to use. Subsequently, 500 μL of the W/O emulsion was coated onto the ITO-coated glass via spin-

coating (POLOS SPIN150i) at various rotational speeds (100, 200, 300, 400, 500, and 600 rpm) and with different numbers of coating layers (1, 2, 4, 6, and 8 layers). After spin-coating, the samples were thermally dried at 60 °C for 5 min.

Anticounterfeiting device preparation

PET substrates (10 cm × 10 cm, 100 cm^2) with single-sided ITO coatings and pristine PET films (10 cm × 10 cm, 100 cm^2) were cleaned with ethanol prior to use. For the fabrication of the dual-band optical modulator-based anticounterfeiting device, a patterned PET film was used as a mask and laminated directly onto the ITO-coated PET substrate. Subsequently, 8 mL of the W/O emulsion was spin-coated at 500 rpm onto the ITO-coated side. For the control group (representing a conventional hydrochromic film), the same W/O emulsion was spin-coated under identical processing conditions onto pristine PET without the low-E layer. Well-defined porous polymer coating patterns were obtained by applying patterned masking tape to both substrates, followed by spin-coating and subsequent careful removal of the masking layer.

Characterisation

The microstructure of porous PMMA was characterised using a scanning electron microscope (FESEM, JEOL JSM-7600F). The average pore size was analysed using ImageJ software by measuring 100 pores from SEM images for each sample, and the mean value with the corresponding standard error was calculated. The pore area fraction was determined by applying binary thresholding to the SEM images using a consistent contrast threshold to distinguish between pore and non-pore regions. Chemical bonding characteristics of the dual-band optical modulator and the control group were confirmed through attenuated total reflectance–Fourier transform infrared (ATR–FTIR, PerkinElmer Frontier). The transmittance modulation of the fabricated dual-band optical modulator under dry–wet states and humidity

conditions was analysed using a UV–Vis–NIR high-sensitivity spectrometer equipped with a point detector (Avantes AvaSpec-ULS2048L StarLine Versatile Fiber-optic Spectrometer and AvaSpecNIR256-2.5-HSC-EVO), with a measurement spot size of 0.5 cm × 0.5 cm. The wet state was achieved by immersing the sample in water for 1 min, followed by thermal drying at 80 °C for 3 min to restore the dry state. The ε_{MIR} value of the samples was measured using a dual-band emissivity measurement instrument (IR-2, Shanghai Chengbo Photoelectric Technology). The ε_{MIR} values were recorded at five distinct locations across each sample, and the average ε_{MIR} value was subsequently calculated. Emissivity spectra were acquired using a PerkinElmer Frontier spectrometer equipped with an integrating sphere. The effective measurement spot size of the FTIR spectrometer was 2 cm × 2 cm. IR images of the dual-band optical modulator under dry–wet states and varying humidity conditions were captured using an IR camera (FLIR E4). Relative humidity (% RH) was controlled using a custom-built environmental chamber equipped with a hygrometer. The durability test was conducted over 30 days, during which the samples were continuously subjected to 80 °C in an oven, UV lamp irradiation, and periodic exposure to a 5 wt% salt solution. At predetermined intervals, the samples were removed, evaluated for modulation performance, and subsequently returned to each respective condition.

Acknowledgment

K.R. expresses sincere gratitude to Nanyang Technological University and the Singapore International Graduate Award. Y.L. is thankful for the funding support from the Global STEM Professorship Scheme sponsored by the Government of Hong Kong Special Administrative Region, Start-up funding from The Chinese University of Hong Kong, 2024 Shenzhen-Hong Kong-Macau Science and Technology Program (Category C) (SGDX20230821094659005), and Innovation and Technology Fund (ITS/221/23). Z.D. and K.R. thanks Centre of Hydrogen

Innovations (CHI) grant CHI-P2023-08 and Academic Research Fund Tier 1 RG159/24 for funding support.

Author Contributions

K.R. contributed to the conceptualisation, investigation, methodology, visualisation, and drafting of the original manuscript; G.W. contributed to investigation and methodology; Z.D. contributed to manuscript review and editing; Y.L. oversaw the conceptualisation, investigation, methodology development, project administration, supervision, visualisation, and manuscript review and editing.

Data Availability

All data are available from the corresponding authors upon reasonable request.

Conflict of Interests

The authors declare that they have no competing interests.

References

1. Sun, H. et al. Integrating biopolymer design with physical unclonable functions for anticounterfeiting and product traceability in agriculture. *Science Advances* **9**, eadf1978 (2023).
2. Sun, Y. et al. Recent progress in smart polymeric gel‐based information storage for anti‐counterfeiting. *Advanced Materials* **34**, 2201262 (2022).
3. Arppe, R. & Sørensen, T. J. Physical unclonable functions generated through chemical methods for anti-counterfeiting. *Nature Reviews Chemistry* **1**, 0031 (2017).

4. Zhang, H. Y. et al. Materials and technologies to combat counterfeiting of pharmaceuticals: current and future problem tackling. *Advanced Materials* **32**, 1905486 (2020).

5. OECD. Mapping Global Trade in Fakes 2025: Global Trends and Enforcement Challenges. (OECD Publishing, 2025).

6. Zhang, C. Y. et al. Conversion of invisible metal-organic frameworks to luminescent perovskite nanocrystals for confidential information encryption and decryption. *Nature Communications* **8**, 1138 (2017).

7. Li, H. et al. Ligand‐induced digital programmable photochromic CdS materials toward dual‐mode light‐printing and information encryption. *Advanced Functional Materials* **34**, 2405877 (2024).

8. Wu, H. et al. Time-resolved encryption from a spiropyran derivative: high-contrasted and multi-state mechanochromism, photochromism and thermochromism. *Chemical Engineering Journal* **469**, 143781 (2023).

9. Li, G. et al. Multimodal, multiband, and multiple anticounterfeiting devices with angle-dependent structural color highly sensitive to temperature. *Research* **8**, 0919 (2025).

10. Cuan, J. et al. Hydro‐photo‐thermo‐responsive multicolor luminescence switching of a ternary MOF hybrid for advanced information anticounterfeiting. *Small* **20**, 2305624 (2024).

11. Sun, W., Wang, J. & He, M. Anisotropic cellulose nanocrystal composite hydrogel for multiple responses and information encryption. *Carbohydrate Polymers* **303**, 120446 (2023).

12. He, X. Y. et al. A multiresponsive functional AIEgen for spatiotemporal pattern control and all‐round information encryption. *Angewandte Chemie* **135**, e202300353 (2023).

13. Zhao, S. W. et al. Single-actuated and fully recyclable phase change materials enabled multiple thermochromism toward information storage and encryption. *Chemical Engineering Journal* **481**, 148698 (2024).

14. Ke, Y. J. et al. Bio‐inspired, scalable, and tri‐mode stimuli‐chromic composite for smart window multifunctionality. *Advanced Functional Materials* **33**, 2305998 (2023).

15. Ke, Y. J. et al. Smart windows: electro‐, thermo‐, mechano‐, photochromics, and beyond. *Advanced Energy Materials* **9**, 1902066 (2019).

16. Bar, N. & Chowdhury, P. A brief review on advances in rhodamine B based chromic materials and their prospects. *ACS Applied Electronic Materials* **4**, 3749-3771 (2022).

17. Abdollahi, A. et al. Photoluminescent and chromic nanomaterials for anticounterfeiting technologies: recent advances and future challenges. *ACS Nano* **14**, 14417-14492 (2020).

18. Wu, Z. H. et al. Highly luminescent and stable inorganic perovskite micro-nanocomposites for crucial information encryption and decryption. *Chemical Engineering Journal* **428**, 131016 (2022).

19. Chen, J. K. et al. Ultrafast and multicolor luminescence switching in a lanthanide-based hydrochromic perovskite. *Journal of the American Chemical Society* **144**, 22295-22301 (2022).

20. Wang, Q. et al. Hydrochromic nanocapsule with real time visual in situ water level sensing function and toughening effect for plastic materials. *Advanced Functional Materials* **34**, 2316271 (2024).

21. Yu, X. Y. et al. Hydrochromic $CsPbBr_3$ nanocrystals for anti‐counterfeiting. *Angewandte Chemie* **132**, 14635-14640 (2020).

22. Han, J. H. et al. Intense hydrochromic photon upconversion from lead‐free 0D metal halides for water detection and information encryption. *Advanced Materials* **35**, 2302442 (2023).

23. Gong, R. et al. Hydrochromic effect of perovskite-polymer composites. *ACS Nano* **18**, 33097-33104 (2024).

24. Yong, J. L. et al. Bioinspired transparent underwater superoleophobic and anti-oil surfaces. *Journal of Materials Chemistry A* **3**, 9379-9384 (2015).

25. Yoo, G. Y. et al. *Diphylleia grayi*-inspired intelligent hydrochromic adhesive film. *ACS Applied Materials & Interfaces* **12**, 49982-49991 (2020).

26. Zhao, C. C. et al. Diphylleia grayi-inspired intelligent temperature-responsive transparent nanofiber membranes. *Nano-Micro Letters* **16**, 65 (2024).

27. Liu, C. X. et al. Hydrogel-coated polydimethylsiloxane with reversible transparency for advanced optical switching. *ACS Nano* **19**, 9017-9028 (2025).

28. Wei, X. Y., Zhang, S. X. A. & Sheng, L. “Enzyme‐Like” spatially fixed polyhydroxyl microenvironment‐activated hydrochromic molecular switching for naked eye detection of ppm level humidity. *Advanced Materials* **35**, 2208261 (2023).

29. Choi, J. & Hyun, J. Hydrochromic film for dynamic information storage using cellulose nanofibers and silica nanoparticles. *Carbohydrate Polymers* **327**, 121663 (2024).

30. Fu, J. H. et al. Hydrochromic visualization of a Keggin-type structure triggered by metallic fluids for liquid displays, reversible writing, and acidic environment detection. *ACS Applied Materials & Interfaces* **13**, 36445-36454 (2021).

31. Xi, G. et al. Water assisted biomimetic synergistic process and its application in water-jet rewritable paper. *Nature Communications* **9**, 4819 (2018).

32. Hu, X. Y. et al. Lightweight and hierarchically porous hydrogels for wearable passive cooling under extreme heat stress. *Matter* **7**, 4398-4409 (2024).

33. Biswas, A. et al. Carbon doped boron nitride nano‐coatings for durable, low emissivity glass windows. *Advanced Materials* **37**, 2507557 (2025).

34. Ali, U., Karim, K. J. B. A. & Buang, N. A. A review of the properties and applications of poly (methyl methacrylate) (PMMA). *Polymer Reviews* **55**, 678-705 (2015).

35. Zidan, H. M. et al. Characterization and some physical studies of PVA/PVP filled with MWCNTs. *Journal of Materials Research and Technology* **8**, 904-913 (2019).

36. Rajendran, S. & Uma, T. Lithium ion conduction in PVC–LiBF4 electrolytes gelled with PMMA. *Journal of Power Sources* **88**, 282-285 (2000).

37. Ramesh, S. et al. FTIR studies of PVC/PMMA blend based polymer electrolytes. *Spectrochimica Acta Part A: Molecular and Biomolecular Spectroscopy* **66**, 1237-1242 (2007).

38. Zhan, Z. S. et al. A novel strategy to improve the flame retardancy and electrical conductivity of polymethyl methacrylate by controlling the configuration

of phosphorus-containing polyaniline@needle coke with magnetic field. *Chemical Engineering Journal* **448**, 137642 (2022).

Figure legends

Figure 1. (a) Schematic illustration of a conventional single-band hydrochromic optical modulator, which provides only a single level of anticounterfeiting functionality in the visible range. (b) Conceptual illustration of a dual-band hydrochromic optical modulator, enabling multi-level anticounterfeiting across the visible, MIR, and ATR–FTIR modes, with each mode selectively revealing different layers of information (the shaded blue and red regions represent the normalised AM1.5 global solar spectrum and the atmospheric transmittance window, respectively). (c) Schematic representation of the fabrication process for the dual-band modulator and the structural configuration of the final device.

Figure 2. (a) (i) Schematic illustration of the structure of the dual-band modulator and SEM images as a function of PMMA concentration: (ii) 1 wt%, (iii) 2 wt%, (iv) 4 wt%, (v) 6 wt%, and (vi) 8 wt% (scale bar: 10 μm). (b) Pore area fraction (%) and average pore size of porous PMMA films as a function of PMMA concentration. (c) FDTD simulation results illustrating transmittance and emissivity modulation behaviour of the dual-band modulator under dry and wet states. (d) Simulated electric field distributions illustrating light propagation at different wavelengths under dry and wet states (i) dry, 500 nm; (ii) dry, 1000 nm; (iii) wet, 500 nm; and (iv) wet, 1000 nm. (e) Simulated electric field distributions at a wavelength of 10 μm under (i) dry and (ii) wet states. The field maps display the lateral (x-axis) and depth (z-axis) directions, with colour representing relative electric field intensity, where red corresponds to higher intensity and blue to lower intensity. The red dotted line represents the porous structure.

Figure 3. (a) Optical transmittance of samples with varying PMMA concentrations in dry and wet states. (b) UV–Vis–NIR transmittance spectra of the 4 wt% PMMA sample in dry and wet states, overlaid with the normalised AM1.5 global solar spectrum (blue-shaded region). (c) Photographs of the 4 wt% PMMA sample in dry and wet states (scale bar: 2 cm). (d) Emissivity values of samples with different PMMA concentrations in dry and wet states. (e) Emissivity spectra of the 4 wt% PMMA sample in dry and wet states, shown together with the normalised AM1.5 atmospheric transmittance spectrum (red-shaded region). (f) IR images of the sample in dry and wet states. (g) Photographs and IR images of the

4 wt% PMMA sample under different RH conditions. (h) RH- and wavelength-resolved (i) transmittance contour map and (ii) emissivity contour map. The x-axis represents RH (%), the y-axis denotes wavelength, and the colour scale indicates (i) transmittance (%) and (ii) emissivity magnitude, with red indicating higher and blue indicating lower values.

Figure 4. (a) Photograph demonstrating the mechanical flexibility of the device. (b) Photographs of (i) the control group and (ii) the prototype in dry and wet states, and (c) corresponding IR images of (i) the control group and (ii) the prototype in the dry state featuring a "★" pattern. (d) Cycling performance of the prototype under repeated drying and wetting cycles. (e) Evolution of ΔT_{lum} of the prototype during 30 days of accelerated aging under three stressors, including high temperature (80 °C, 60% RH, yellow curve), 365 nm UV irradiation (blue curve), and 5 wt% saltwater exposure (red curve). (f) Photographs and IR images of (i) the control group with "♥" patterns and (ii) the prototype incorporating both "♥" and "★" patterns simultaneously. (g) UV–Vis–NIR transmittance and emissivity spectra of (i) the control group and (ii) the prototype in dry and wet states, presented alongside the normalized AM1.5 global solar spectrum (blue shading) and the atmospheric transmittance window (red shading). (h) ATR–FTIR reflectance spectra of the control and the prototype, with arrows denoting characteristic vibrational absorption peaks.